COMPARISON OF FREQUENCY AND TIME DOMAIN IDENTIFICATION OF A HELICOPTER IN HOVER

Natalia Cejudo Trillo Graduate Student

Ongun Hazar Aslandoğan Research Associate

İlkay Yavrucuk Professor

Institute for Rotorcraft and Vertical Flight
Technical University of Munich
Munich, Germany

ABSTRACT

This paper focuses on frequency domain system identification of a full-scale helicopter under both hover and forward flight conditions and comparison of the results with time domain identification. A high fidelity nonlinear simulation model resembling a 3T class helicopter is employed. Frequency-sweep input signals are applied to generate the required input-output datasets. The time domain signals are transformed into the frequency domain using the Discrete Fourier Transform, along with conditioning and composite windowing techniques to ensure high accuracy and reliability. A state space system based on a six degree of freedom quasi steady linear model is identified using the output error method combined with the Levenberg-Marquardt algorithm. To account for higher-order dynamics, time delays are introduced between inputs and outputs. In addition, the frequency domain based identified system is compared against an independently time domain identified model using data from the same truth model. The results demonstrate high identification accuracy, with the key aerodynamic derivatives estimated within a consistent and comparable range.

NOTATION

*

Symbols

A,B,C,D state space representation matrices

C_ε normalized random error constant

$\overline{CR}$ normalized Cramer-Rao bound

f frequency, Hz

$G_{ij\cdot r!}$ general conditioned spectral density function

$\tilde{G}_{x_ix_j}$ input cross spectral density function

G_{xx_c} composite input autospectral density function

$\tilde{G}_{xx}$ input autospectral density function

$\widehat{G}_{xx}$ weighted averaged input autospectral functions

$\tilde{G}_{xy}$ cross spectral density function

G_{xy_c} composite cross spectral density function

G_{yy_c} composite output autospectral density function

$\tilde{G}_{yy}$ output autospectral density function

H frequency response

H_c composite frequency response function

J composite windowing cost function

L_{rj} constant-parameter linear frequency response function

N number of samples

n_d number of windows

n_i number of inputs

p,q,r rool,pitch and yaw rates, deg/s

T length of the segments of the recorded data, s

T_r total length of the recorded data, s

$\mathbf{u}$ control input vector

u_n input time based signal, s

u,v,w translational velocities in body fixed frame, ft/s

W_i weighting function

$\mathbf{x}$ state vector

$X(f)$ input Fourier coefficient

y output vector

$Y(f)$ output Fourier coefficient

z_n output time based signal

$\tilde{\gamma}^2_{x_i x_j}$ cross-control coherence function

$\tilde{\gamma}^2_{x_i y\cdot(n_i-1)!}$ partial coherence function

$\tilde{\gamma}^2_{xy}$ coherence function

γ_{xy_c} composite coherence function

$\tilde{\gamma}^2_{y:p!}$ multiple coherence function

Δt time step,s

δ_{col} collective control, %

δ_{lat} lateral cyclic control, %

δ_{lon} longitudinal cyclic control, %

δ_{ped} pedal control, %

ε error function

ε_r normalized random error

$\varepsilon_{r\cdot(n_i-1)!}$ conditioned random error

θ, ϕ, ψ pitch, roll and yaw angles, deg

*

Acronyms

AEE Allowable Error Envelopes

CIFER Comprehensive Identification from Frequency Responses

DFT Discrete Fourier Transformation

DoF Degree of Freedom

MIMO Multi Input Multi Output

MUAD Maximum Unacceptable Amplitude Deviation

SISO Single Input Single Output

INTRODUCTION

Accurate modeling of flight dynamics is fundamental for understanding an aircraft's performance, stability and control characteristics. These insights are essential for various applications, including flight control system design (Ref. 1), performance evaluation and handling qualities analysis (Ref. 2). A core method in this process is system identification, which derives predictive models from experimental data, capturing real world vehicle behavior and underlying dynamics (Ref. 3). System identification can be conducted in both time and frequency domains, each offering distinct advantages and presenting specific limitations.

Time domain identification involves fitting differential equation models to measured time domain data. This approach enables the identification of a state-space model, including aerodynamic derivatives and time delays, as demonstrated in the time domain analysis conducted by Aslandogan et al. (Ref. 3), which focuses on the system identification of the same 3T class helicopter truth model as in the present frequency domain investigation. Nevertheless, this approach entails significant computational demands and relies heavily on strong a priori assumptions regarding the model structure, system order and relevant nonlinearities. Furthermore, owing to the inherent non-uniqueness of state space representations, achieving an accurate fit in the time domain does not necessarily guarantee precise frequency domain behavior. Such methods tend to emphasize low-frequency dynamics, as a result of the higher concentration of data points in that range (Ref. 4).

Frequency domain methods rely on spectral analysis to extract the frequency response between selected input output pairs. This approach seeks to minimize the error between measured data and the model by comparing phase and magnitude, typically presented in the form of Bode plots. They are particularly useful for control system design, pilot handling evaluation and transient analysis of novel aircraft configurations (Ref. 5). These methods provide higher fidelity in the mid and high frequency ranges, which are essential for capturing transient dynamics associated with pilot inputs. Moreover, they handle noisy data more effectively. Due to their non-parametric nature, they generally require fewer prior assumptions compared to time domain methods. However, they tend to be less accurate in modeling low frequency and steady state behaviors. Furthermore, because the frequency response represents a linearized system, these methods are less effective in flight regimes dominated by strong nonlinearities such as stall or autorotation (Ref. 6).

The origins of frequency domain system identification can be traced back to the early 1950s, with foundational work on transfer function modeling by Greenberg et al. (Ref. 7) and Shinbrot et al. (Ref. 8). Since then, the field has evolved significantly. A pivotal development was the development of CIFER®, a specialized software tool developed by NASA and the U.S. Army, which has become a widely used tool for frequency domain system identification (Ref. 9).

Numerous studies have demonstrated the effectiveness of frequency domain methods across various flight regimes. These techniques have been successfully applied to diverse aircraft, including the XV-15 tiltrotor, Bell 214ST, and Bo-105 helicopters, highlighting their capability to accurately capture complex, high order dynamic behaviors, as documented in works by Tischler et al. (Refs. 4, 10, 11) and Lawler et al. (Ref. 12). Berger et al. (Ref. 13) provide a comprehensive overview of the evolution of frequency domain system identification at the U.S. Army Combat Capabilities Development Command Aviation & Missile Center, emphasizing its pivotal role in contemporary rotorcraft modeling. Additionally, Wu et al. (Ref. 14) performed a comparative analysis of time and frequency domain identification methods on a small scale helicopter, demonstrating that both approaches yield accurate models, each presenting distinct advantages and limitations depending on the specific flight regime and application.

Transformation of test data from time domain to frequency domain is a crucial stage in frequency domain identification, where appropriate signal conditioning and other preprocessing techniques are vital to ensure accurate frequency response estimation. Tischler and Tomashofski (Ref. 15) underline the significance of signal conditioning for the precise identification of MIMO systems, particularly in complex high order rotorcraft models such as the SH-2G. Effective system identification requires selecting an appropriate model structure that aligns with the frequency range of interest, the degree of dynamic coupling, the intended application and the specific characteristics of the vehicle's dynamics. Significant contributions to the modeling of rotor and engine dynamics for the ACT/FHS helicopter have been made by Seher-Weiss through extensive studies (Refs. 16–18), which also offer valuable insights into rotor flapping and vertical motion.

This study presents a comprehensive frequency domain system identification framework applied to a full scale helicopter simulation model. Starting from time domain simulation data, essential preprocessing steps, such as signal conditioning and composite windowing, are applied to obtain reliable frequency domain signals. Transfer functions are estimated using the output error method combined with the Levenberg-Marquardt algorithm. The discrepancy between the identified and true systems is assessed through Allowable Error Envelopes (AEE) (Ref. 19) and Maximum Unnoticeable Added Dynamics (MUAD) (Ref. 20) bounds to validate the identified model. Furthermore, this work emphasizes the inherent challenges in frequency domain system identification, strengths, and limitations of the approach. By examining these aspects, it advances the understanding of frequency domain system identification and supports its practical application in rotorcraft modeling. The identified model is subsequently compared in the time domain using 3211 and 2311 input profiles to demonstrate its effectiveness. Finally, a comparative analysis is conducted against the time domain identification results previously obtained by Aslandogan et al. (Ref. 3), employing the same high-fidelity helicopter truth model. This comparison offers valuable insights into the respective advantages and limitations of each approach.

FREQUENCY DOMAIN METHODOLOGY

Data Characteristics

Accurate system identification necessitates that the targeted dynamic characteristics are sufficiently excited within the dataset. Consequently, the relevant frequency range and dynamic couplings must be clearly defined prior to data acquisition. In this study, data were generated using a high-fidelity nonlinear simulation model of a 3T class helicopter (Refs. 3,21), employing frequency sweep inputs to ensure excitation throughout the frequency bandwidth of interest. On the other hand, 3211 and 2311 type multistep inputs are used for time domain validation. During data generation, low frequency controllers in the secondary axes are employed to prevent divergence far from the trim region.

Frequency sweeps apply sinusoidal signals with increasing frequency, ensuring uniform spectral excitation across the full range of interest and enabling comprehensive dynamic characterization. In contrast, multistep inputs such as 3211 and 2311 are shorter and concentrate energy within targeted frequency bands, thereby optimizing spectral density based on prior dynamic estimates and making them more suitable for time domain identification techniques (Ref. 6).

Analyzing the input output response of a Multi Input Multi Output (MIMO) system requires accounting for the interdependence of control inputs. In a helicopter, these inputs are the longitudinal and lateral cyclic controls, collective pitch and pedals. In an ideal scenario, assessing the response of each output to a given input requires actuating solely that input, ensuring the output's behavior is attributed exclusively to it. However, in practice, pilots must operate multiple controls simultaneously to ensure flight stability and maneuver execution. As shown in Figure 1, even when each input was alternately prioritized during data collection, the other controls were not held stationary, highlighting inherent input correlation and the need for appropriate signal conditioning during analysis.

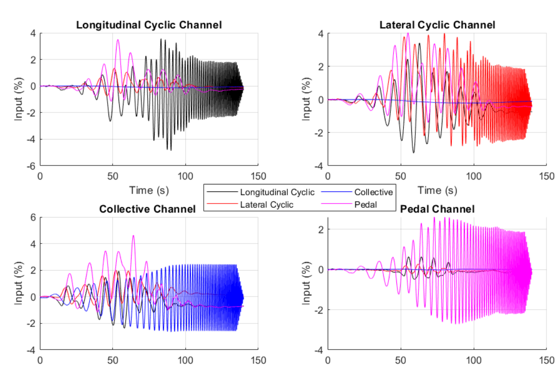

Figure 1. Frequency sweep inputs given to each channel in hover.

Transformation of the Time Domain Data to Frequency Domain

The Discrete Fourier Transform (DFT) is applied to the dataset, which consists of discrete time samples. To improve the accuracy of the estimated spectral functions, the complete signal of duration T_r is partitioned into segments of equal length T. This segmentation enables the application of the averaging methodology described by Bendat et al. (Ref. 22), which serves to attenuate the errors introduced by measurement noise in both input and output signals, typically arising from external disturbances during flight testing in real life applications. Furthermore, segmentation facilitates the implementation of time history windowing, a necessary step to mitigate side lobe leakage due to the inherently non-periodic nature of recorded or simulated flight data.

The DFT is computed for each segment. To address the non-periodicity of the data, each segment is multiplied with a Hanning window, which is commonly adopted in flight dynamics applications owing to its smooth tapering to zero at both ends. This ensures continuity between adjacent segments and suppresses spectral leakage. The resulting expressions are given by Eq.1 and Eq. 2, where the subscript i denotes the segment index. Additional accuracy is achieved by allowing for overlapping segments, which improves the resolution of the spectral functions. The corresponding spectral functions are derived from these transformed signals, as defined in Eq.3, Eq.4, Eq. 5 and Eq 6.

$$X_i(f) = \Delta t \sqrt{\frac{8}{3}} \sum_{n=0}^{N-1} u_n (1 - cos(\frac{\pi n}{N})) exp[\frac{j2\pi kn}{N}] \tag{1}$$

$$Y_i(f) = \Delta t \sqrt{\frac{8}{3}} \sum_{n=0}^{N-1} z_n (1 - cos(\frac{\pi n}{N})) exp[\frac{j2\pi kn}{N}] \tag{2}$$

The number of segments n_d is directly determined by the chosen window size. Small windows increase the number of segments available for averaging, thereby enhancing noise suppression and improving identification accuracy at higher frequencies. However, this advantage comes at the cost of raising the effective minimum frequency, which reduces the information content at lower frequencies. Conversely, larger windows capture more detailed information and provide better resolution at lower frequencies, but they decrease the number of segments for averaging, resulting in increased random error and greater noise influence at higher frequencies. To manage the trade-offs between these effects, composite windowing as highlighted in (Ref. 6) is implemented.

The input autospectrum (Eq.3) represents the distribution of excitation power across frequencies. Similarly, the output autospectrum (Eq. 4) describes how the system response power is distributed over the frequency range. The cross spectrum (Eq. 5) quantifies the frequency dependent transfer of power between input and output, including both magnitude and phase information essential for identifying system dynamics. The input cross spectral function (Eq. 6) plays a critical role in the formulation of conditioned frequency response functions.

$$\tilde{G}_{xx} = \frac{1}{n_d} \sum_{k=1}^{n_d} (\frac{2}{T} |X(f)|^2)_k \tag{3}$$

$$\tilde{G}_{yy} = \frac{1}{n_d} \sum_{k=1}^{n_d} (\frac{2}{T} |Y(f)|^2)_k \tag{4}$$

$$\tilde{G}_{xy} = \frac{1}{n_d} \sum_{k=1}^{n_d} (\frac{2}{T} |X^*(f) Y(f)|)_k \tag{5}$$

$$\tilde{G}_{x_i x_j} = \frac{1}{n_d} \sum_{k=1}^{n_d} (\frac{2}{T} |X_i^*(f) X_j(f)|)_k \tag{6}$$

The definition of two coherence metrics is essential for evaluating the reliability of frequency domain identification. The coherence function (Eq. 7) measures the degree of linear dependence between input and output signals. It ranges from 0 to 1, with values close to 1 indicating a highly linear and noise free relationship, where 1 represents the ideal case of a fully linear system. In practice, however, the coherence rarely reaches this ideal, due to noise in output measurements, nonlinear effects, and interferences from multiple inputs, as highlighted in (Ref. 22). Typically, a stable coherence value above 0.6 is considered sufficient for robust system identification, as noted in (Ref. 6).

$$\tilde{\gamma}^2_{xy} = \frac{|\tilde{G}_{xy}|^2}{|\tilde{G}_{xx}| |\tilde{G}_{yy}|} \tag{7}$$

Cross control coherence, defined in Eq. 8, measures the correlation between inputs, from 0, uncorrelated, to 1, fully correlated. A value of 1 makes it impossible to identify individual input-output pairs, while 0 simplifies MIMO identification to a set of decoupled SISO systems. For a well-conditioned process, average cross control coherence should remain below 0.5.

$$\tilde{\gamma}^2_{x_i x_j} = \frac{|\tilde{G}_{x_i x_j}|^2}{|\tilde{G}_{x_i x_i}| |\tilde{G}_{x_j x_j}|} \tag{8}$$

Lastly, the random error, defined in Eq. 20, quantifies the normalized random error expected in the computed frequency response. A key factor is the overlap percentage between segments; increasing overlap to 80% significantly reduces this error (Ref. 6). High random error, seen as magnitude and phase fluctuations, can deteriorate the accuracy of the spectral estimates.

$$\varepsilon_r = C_\varepsilon \frac{[1 - \gamma^2_{xy}]^{1/2}}{|\gamma_{xy}| \sqrt{2 n_d}} \tag{9}$$

Conditioning

In MIMO system identification, the control input related to the studied input-output pair is called the primary input, while all others are the secondary inputs. Once influence of the secondary inputs on the primary input is quantified, their effect can be removed with conditioning. This procedure is defined as isolating the direct relationship between the primary input and the output of the input-output pair under study by Bendat and Piersol (Ref. 22).

Conditioned spectral values are computed using the algorithm in Eq. 10, as defined by Bendat and Piersol (Ref. 22), which applies to both diagonal ($i = j$) and off-diagonal ($i \neq j$) terms. The method remains effective regardless of input correlation, reducing to classical SISO results when inputs are uncorrelated. An alternative approach proposed by Otnes et al. (Ref. 23) was also implemented in this study, yielding equivalent outcomes.

$$G_{ij.r!}(f_k) = G_{ij.(r-1)!}(f_k) - L_{rj}(f_k)G_{ir.(r-1)!}(f_k), \quad L_{rj}(f_k) = \frac{G_{rj.(r-1)!}(f_k)}{G_{rr.(r-1)!}(f_k)} \tag{10}$$

Figure 2 and Figure 3 demonstrate the effectiveness of the conditioning procedure. The dataset was generated from a noise free state space model with two outputs and three inputs, using forward Euler integration. Not only the primary input was excited, but the secondary inputs were also varied, although in a smaller magnitude. This introduced fluctuations in the states in both magnitude and phase, particularly at higher frequencies. Conditioning significantly diminished the impact of the secondary inputs, yielding a response that closely approximates the ideal case, where only the primary input is active. As part of the conditioning process, two additional spectral metrics are introduced, the partial coherence $\gamma^2_{x_iy\cdot(n_i-1)!}$ and the multiple coherence $\gamma^2_{y:p!}$. The partial coherence, Eq.11, quantifies the proportion of the conditioned output spectrum that is linearly attributable to the conditioned primary input, after the influence of all secondary inputs has been removed (Ref. 22). This measure provides a more accurate characterization of the input-output linear relationship than traditional coherence, which can produce misleading results. For instance, in cases where the primary input has no direct linear influence on the output, but is highly correlated

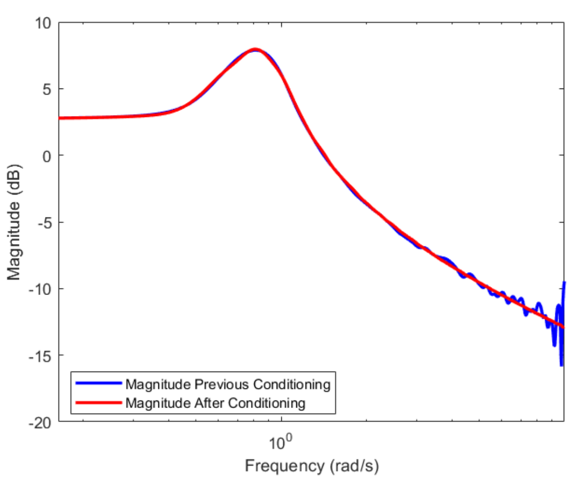

Figure 2. Magnitude before and after conditioning.

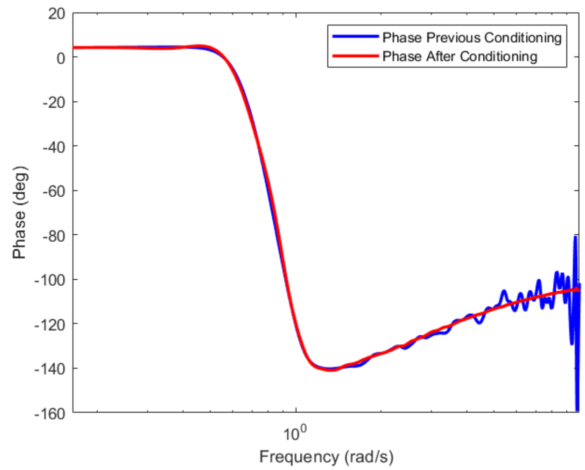

Figure 3. Phase before and after conditioning.

with another input that does, the standard coherence function may indicate a strong linear relationship. In contrast, partial coherence correctly accounts for such dependencies by isolating the influence of the primary input, thereby revealing the true nature of the interaction and resulting in lower coherence values.

$$\gamma^2_{x_iy\cdot(n_i-1)!} = \frac{\left|G_{x_iy\cdot(n_i-1)!}\right|^2}{\left|G_{x_ix_i\cdot(n_i-1)!}\right|\left|G_{yy\cdot(n_i-1)!}\right|} \tag{11}$$

The multiple coherence, Eq.12, quantifies the fraction of the output that is linearly related to all considered inputs in the conditioning analysis. A multiple coherence value less than 1 may result from several factors, including measurement noise at the output, the presence of nonlinearities, or the omission of relevant secondary inputs from the model. For the results to be considered reliable, the multiple coherence should be sufficiently close to unity (Ref. 22). A low value may indicate that the model requires refinement, either by incorporating additional inputs or by accounting for nonlinear system behavior.

$$\gamma^2_{y:p!} = \sum_{i=1}^{p} \gamma^2_{x_iy\cdot(i-1)!} \tag{12}$$

The conditioned random error is computed from the conditioned spectral functions with the same definition as before, as shown in Eq. 13.

$$\varepsilon_{r\cdot(n_i-1)!} = C_\varepsilon \frac{\left[1-\gamma^2_{x_iy\cdot(n_i-1)!}\right]^{1/2}}{\left|\gamma_{x_iy\cdot(n_i-1)!}\right|\sqrt{2n_d}} \tag{13}$$

Once conditioning is applied, the real input–output dynamics can be examined across window sizes. For brevity, the $(n_i - 1)!$ index is omitted hereafter.

Composite Windowing

Composite windowing addresses the limitations of fixed window sizes during the transformation of the time domain data to frequency domain by combining multiple windows, each suited to different frequency ranges. This enhances the accuracy, reliability and robustness of frequency response estimates across the spectrum. As highlighted by Tischler et al. (Ref. 6), the method improves the accuracy of system identification by maintaining high coherence and reducing random error throughout the frequency range. To integrate the results into a smooth spectral representation, weighted averaging is employed, where the weighting function W_i (Eq. 14) is defined inversely to the random error, favoring the most reliable estimates for each frequency range segment.

$$W_i = \left(\frac{(\varepsilon_r)_i}{(\varepsilon_r)_{min}} \right)^{-4} \tag{14}$$

The weighted average input autospectral density is defined in Eq. 15. The composite spectral functions are obtained by minimizing the cost function J (Eq. 16). This cost function takes the conditioned spectral functions across all window sizes, their weighted average and the resulting composite spectral functions, and coherence metrics into account. The inclusion of the composite coherence, average coherence and partial coherence introduces nonlinear dependencies, making an iterative solution necessary to ensure convergence.

$$\widehat{G_{xx}} = \frac{\sum_{i=1}^{n_w} W_i^2 G_{xx_i}}{\sum_{i=1}^{n_w} W_i^2} \tag{15}$$

$$\begin{aligned} J = \sum_{i=1}^{n_w} W_i \Bigg(& \left(\frac{G_{xx_c} - G_{xx_i}}{\widehat{G_{xx}}} \right)^2 + \left(\frac{G_{yy_c} - G_{yy_i}}{\widehat{G_{yy}}} \right)^2 \\ & + \left(\frac{Re(G_{xy_c}) - Re(G_{xy_i})}{Re(\widehat{G_{xy}})} \right)^2 + \left(\frac{Im(G_{xy_c}) - Im(G_{xy_i})}{Im(\widehat{G_{xy}})} \right)^2 \\ & + 5.0 \left(\frac{\gamma^2{}_{xy_c} - \gamma^2{}_{xy_i}}{\widehat{\gamma^2_{xy}}} \right)^2 \Bigg) \end{aligned} \tag{16}$$

Assuming that noise primarily affects the output measurements while the inputs remain noise-free, the frequency responses can be obtained using the expression given in Eq. 17.

$$H_c = \frac{G_{xy_c}}{G_{xx_c}} \tag{17}$$

Mathematical Model Structure

A state-space linear 6-DoF model is used, assuming a quasi-steady rotor response, an acceptable simplification for helicopters with low flapping stiffness where rotor dynamics can be treated as instantaneous. The linear model relates perturbations in body velocities (u, v, w), angular rates (p, q, r) and Euler angles (ϕ, θ, ψ) to perturbations in control inputs $(\delta_{\text{lon}}, \delta_{\text{lat}}, \delta_{\text{col}}, \delta_{\text{ped}})$. To account for transient rotor effects, time delays are introduced to the inputs, allowing one delay per transfer function if necessary. Since simulated data are used, the states are assumed to be fully measured, which reduces C to identity matrix and sets D as a zero matrix when the sate-space model is expressed as Eq.18. Details on the derivation of the linear state space model and its underlying assumptions can be found in (Ref. 24) and (Ref. 25). From the defined system, the transfer functions can easily be obtained using Eq.19. In this case, the unknowns are directly the aerodynamic derivatives.

$$\begin{aligned} \dot{\mathbf{x}} &= A\mathbf{x} + B\mathbf{u} \\ \mathbf{y} &= C\mathbf{x} + D\mathbf{u} \end{aligned} \tag{18}$$

$$T(s) = C(sI - A)^{-1}B + D \tag{19}$$

The model structure employed in this work is adapted from (Ref. 3), where the state-space model structure is determined using a Hessian matrix based model reduction routine, using the Cramer-Rao bounds and insensitivities as the criteria to remove redundant derivatives (Ref. 6). While rotorcraft models can reach high orders when accounting for rotor-fuselage interactions, practical models prioritize the minimal structure necessary to accurately capture the system response within the target frequency band. Overfitting by using excessive model order may introduce non-physical behavior and reduce interpretability. Time delays on cyclic inputs were introduced to represent physical lags or to approximate unmodeled dynamics.

For a rotorcraft operating in hover or at low forward speeds, the dominant input–output channels typically include pitch rate to longitudinal cyclic input (q/δ_{lon}), roll rate to lateral cyclic input (p/δ_{lat}), and yaw rate to pedal input (r/δ_{ped}). In the vertical axis, the relationship between vertical speed and collective input (w/δ_{col}) is commonly examined. To accurately capture the system's dynamics, key off-axis responses must also be included. The roll response to longitudinal cyclic (p/δ_{lon}) and pitch response to lateral cyclic (q/δ_{lat}) account for pitch–roll coupling induced by rotor gyroscopic effects. Lateral speed due to pedal input (v/δ_{ped}) captures side-force contributions from fuselage and tail rotor interactions, while yaw rate in response to collective input (r/δ_{col}) reflects torque induced effects on tail rotor. Incorporating these off-axis terms is essential to represent the the longitudinal-lateral coupling inherent to helicopter flight dynamics and ensure a comprehensive system identification. Additionally, the input-output pairs u/δ_{lon}, v/δ_{lat}, r/δ_{lat}, p/δ_{col}, q/δ_{col} and v/δ_{ped} are included in the cost function due to their high coherence values.

Identification

For the identification of the system, the output error optimization loop coupled with the Levenberg-Marquardt algorithm, presented by Aslandogan et al. (Ref. 3), was used. The output error method focuses on reducing the error between the real system frequency response and the mathematical model by iteratively updating the unknown system parameters. The Levenberg-Marquardt algorithm helps prevent intermediate divergence of the optimization loop and contributes to parameter updates in the steepest descent direction.

Validation of the Identified Model

To evaluate estimation accuracy, the error function in Eq.20 compares the model responses to the true system. Its magnitude and phase are assessed against two criteria: the MUAD bounds (Ref. 20), based on handling qualities and pilot perceptibility, and the AEEs, proposed by Mitchell et al. (Ref. 19), derived from pilot-in-the-loop testing. Staying within these bounds ensures both identification accuracy.

$$\varepsilon(f) = \frac{H_{sim}(f)}{H_{flight}(f)} \tag{20}$$

Additionally, time domain validation is carried out by comparing the identified model's response to simulation data generated using standard 3211 and 2311 input profiles.

FREQUENCY DOMAIN IDENTIFICATION RESULTS

This section presents results in hover flight from the state-space identified system, where the unknown coefficients are directly the aerodynamic derivatives. The results also include comparisons with the identified system without time delays in cyclic inputs. It is important to note that the input data used in this study exhibit significant cross-coherence, often exceeding the 0.5 threshold commonly accepted as the upper limit for reliable conditioning. This characteristic must be carefully considered in the interpretation and analysis of the identification outcomes. The values of the helicopter at trim conditions at hover flight at sea level are listed in Table 1. Figures 4 and 5, show the roll and pitch responses to the longitudinal cyclic control. Figure 4 shows the frequency response errors in the off-axis response of p/δ_{lon}. A time delay to the input is introduced to account for the rotor response lag, improving the estimation accuracy, particularly in phase at higher frequencies. Nevertheless, a localized discrepancy remains within a narrow frequency bandwidth. The composite partial coherence for the q/δ_{lon} channel remains stable and close to 1 across most of the frequency range, indicating a strong linear relationship. In contrast, the coherence for the p/δ_{lon} pair is slightly lower but consistently above the 0.6 threshold, ensuring reliable identification ((Ref. 6)). As shown in the figures, both estimated transfer functions align well with the true system with time delays. Estimation errors are generally low, increasing where coherence drops. For the lateral cyclic input, the p/δ_{lat} pair also exhibits high coherence, remaining

Table 1. Trimmed state values at hover.

Parameter	Value	Parameter	Value
u_0	0 ft/s	δ_{long_0}	66.18%
v_0	0 ft/s	δ_{lat_0}	52.65%
w_0	0 ft/s	δ_{coll_0}	64.13%
ϕ_0	-2.87 deg	δ_{ped_0}	37.45%
θ_0	6.76 deg	Total Mass	2800.0 kg

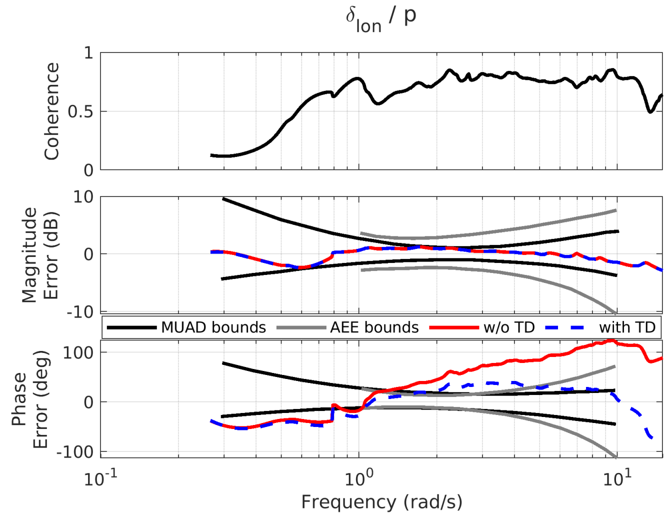

Figure 4. Frequency domain identification of p/δ_{lon} in hover.

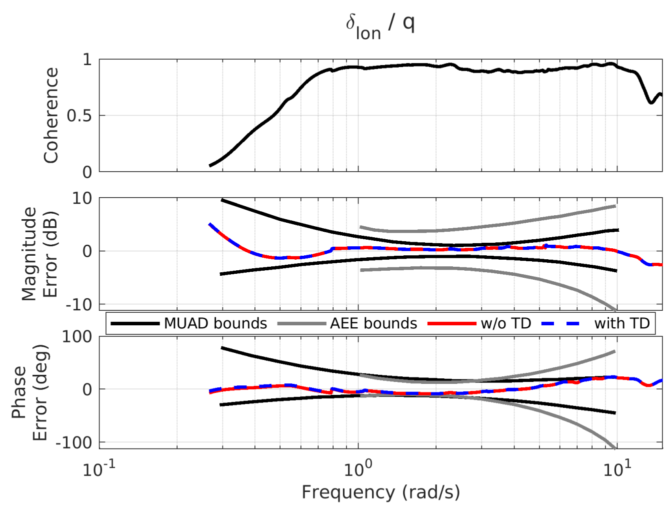

Figure 5. Frequency domain identification of q/δ_{lon} in hover.

close to 1 throughout most of the frequency spectrum. In contrast, the q/δ_{lat} coherence is lower, however, it stays above the value of 0.6. As seen in Figure 6 and Figure 7, both estimated transfer functions show good agreement with the true model. The p/δ_{lat} response remains within the confidence bounds, while the q/δ_{lat} estimation shows larger deviations at higher frequencies, where the errors diminish significantly with introduced time delay in the response pair. The response pairs for collective and pedal channels show satisfactory results where the errors are within the validation bounds. The results for these channels are presented in the following sections.

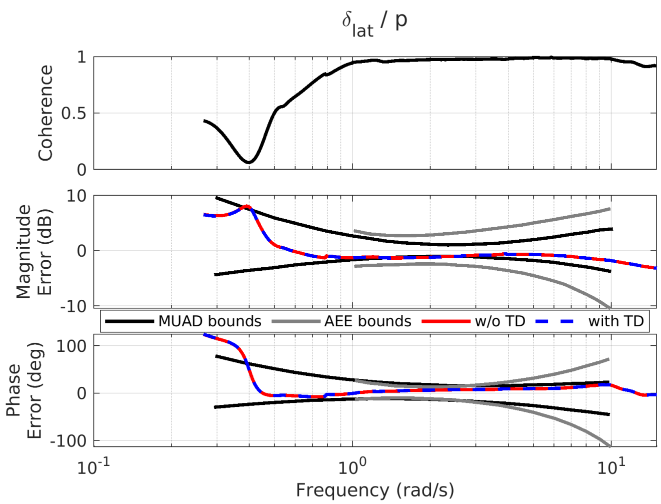

Figure 6. Frequency domain identification of p/δ_{lat} in hover.

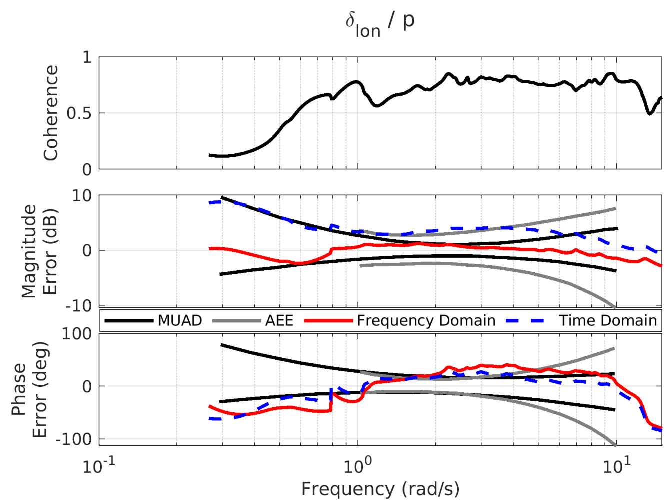

Figure 8. Comparison of identification of p/δ_{lon} in frequency domain

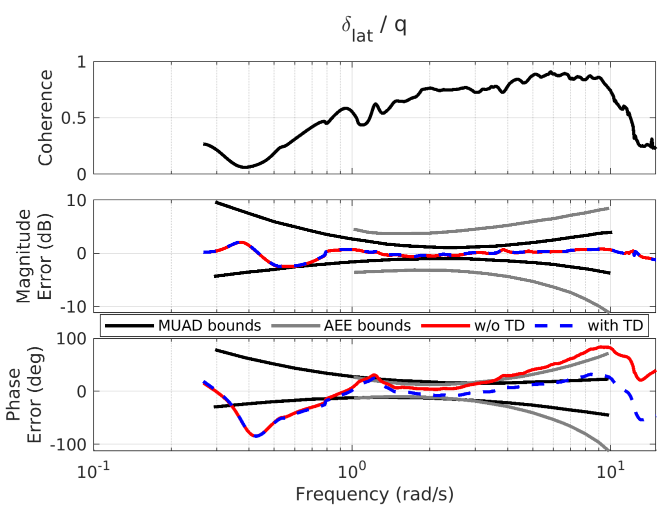

Figure 7. Frequency domain identification of q/δ_{lat} in hover.

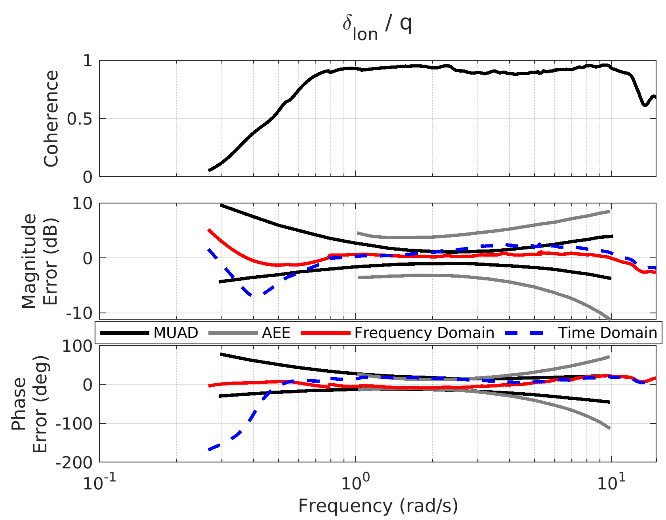

Figure 9. Comparison of identification of q/δ_{lon} in frequency domain

COMPARISON OF FREQUENCY DOMAIN AND TIME DOMAIN IDENTIFICATION RESULTS

This section presents a comparison between the system identified in frequency domain in this paper and the system identified in the time domain by Aslandogan et al. (Ref. 3). Both identification approaches employ the data generated from the same nonlinear truth model, where time domain approach used multistep maneuvers and frequency domain approach used frequency sweep maneuvers for identification. The model structure is obtained through a systematic model reduction routine carried out in time domain in (Ref. 3). The frequency response calculations are carried out with the conditioning and composite windowing framework outlined in this paper for both identified models.

Figures 8 and 9 show the roll and pitch responses to longitudinal cyclic control and Figures 10 and 11 show the same responses to lateral cyclic control. When the responses to longitudinal cyclic channel are considered, the on-axis pitch rate response remains within the MUAD and AEE error bounds over the high coherence frequency bandwidth. In contrast, the off-axis roll rate response exhibits lower coherence across the frequency range of interest. In terms of magnitude error, the time domain identified model slightly exceeds the bounds, whereas the frequency domain identified model remains within. For phase errors, however, the opposite trend is observed, where the frequency domain model performs slightly worse. This discrepancy arises from the different error definitions used in the two identification approaches and the distinct input-output response pairs considered during the identification procedure. While the time domain identification takes all state responses into account, frequency domain identification focuses on the input-output pairs with high coherence values, as highlighted in the chapter describing the mathematical model structure.

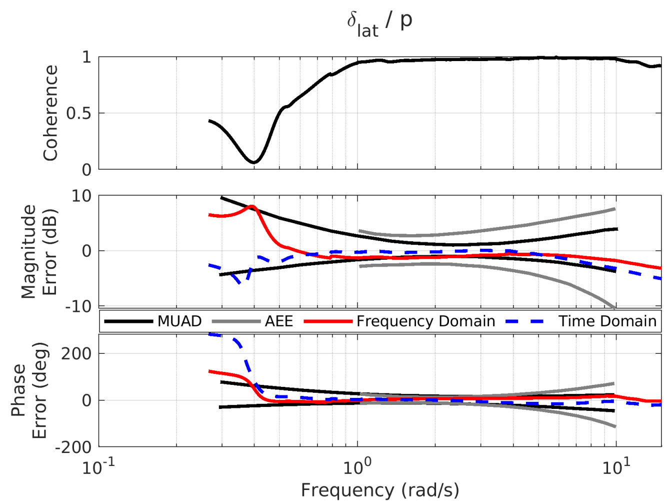

Figure 10. Comparison of identification of p/δ_{lat} in frequency domain

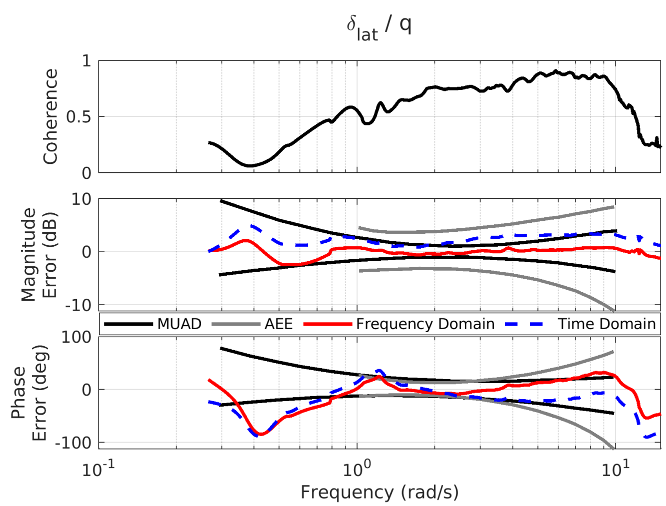

Figure 11. Comparison of identification of q/δ_{lat} in frequency domain

Moreover, the maximum likelihood output error method employed for identification is highly sensitive to initial conditions, which strongly influence the direction of parameter updates. Consequently, the two solutions converge to slightly different local minima.

Figures 12 and 13 show the vertical velocity and yaw rate responses to collective control, and Figures 14 and 15 show the lateral velocity and yaw rate responses to pedal control. For both time domain and frequency domain responses, the errors fall within the validation bounds, where all responses show high coherence throughout the frequency range. Both identified models are also compared in time domain maneuvers consisting of 3211 and 2311 type multistep inputs. Figures 16, 17, 18 and 19 provide a brief overview of time domain responses to 2311 type inputs in different channels.

Figures 16 and 17 show pitch and roll rate responses to longitudinal and lateral cyclic inputs, respectively. Figure 18

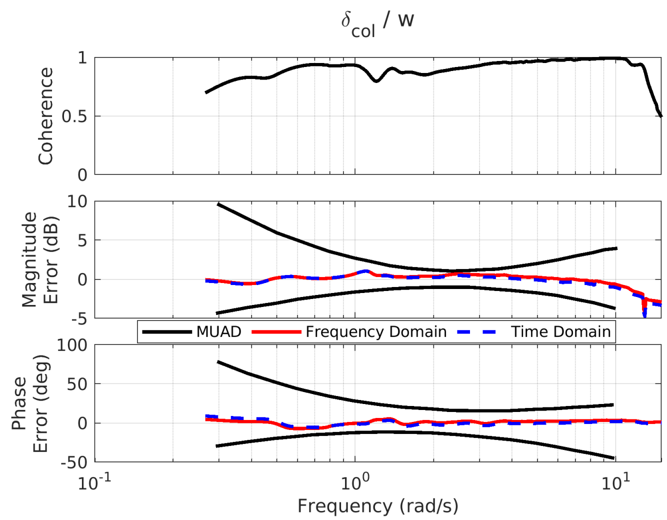

Figure 12. Comparison of identification of w/δ_{col} in frequency domain

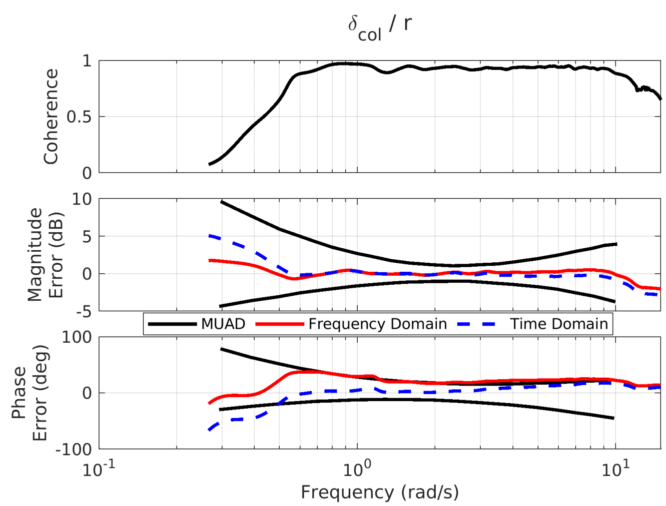

Figure 13. Comparison of identification of r/δ_{col} in frequency domain

presents vertical speed and yaw rate responses to collective input, and figure 19 shows lateral speed and yaw rate responses to pedal input. In these comparisons, It is observed that the model identified in time domain follows the truth model response with greater accuracy, as the time domain model was identified using the multistep maneuver dataset. Nevertheless, the errors in the time domain fit of the frequency domain identified model was found to be adequate.

Finally, the stability and control derivatives identified with time domain and frequency domain methodologies have been compared along with their respective Cramer-Rao bounds. The Cramer–Rao bounds define the minimum standard deviation of an identified parameter. They quantify the sensitivity of the cost function to variations in that parameter. Large Cramer–Rao values indicate correlation among parameters. When normalized by the corresponding parameter value, a guideline of $\overline{\mathrm{CR}}_i \leq 20\%$ is sought (Ref. 6) during the process

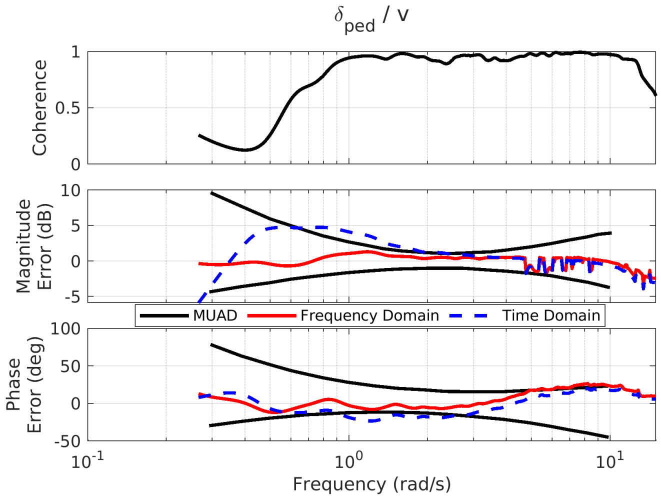

Figure 14. Comparison of identification of v/δ_{ped} in frequency domain

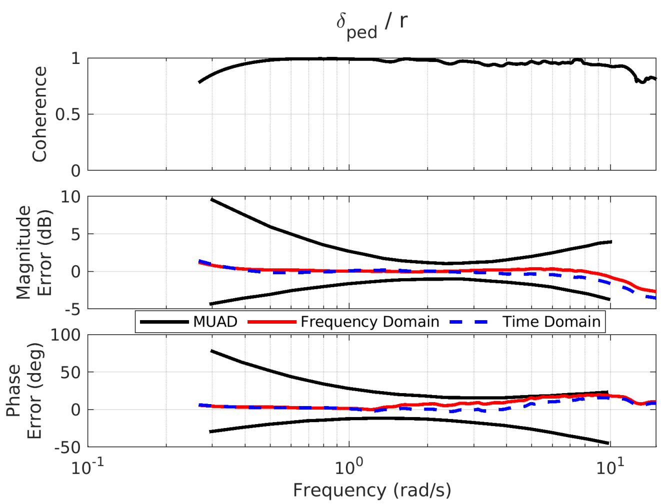

Figure 15. Comparison of identification of r/δ_{ped} in frequency domain

of model structure determination.

The Table 2 presents the stability derivatives identified with both approaches. Note that some of the aerodynamic derivatives were either removed from or added to the model structure following the examinations of the frequency responses and the initial identification results. The table indicates overall good agreement between the two approaches, where the important aerodynamic derivatives have values with physically meaningful signs and order of magnitudes. However, since the model structure determination is carried out within the time domain methodology, some of the derivatives with slightly larger Cramer-Rao bounds still remain in the model structure. An example is the drag derivative X_u, which has a normalized Cramer–Rao value of 9.7 and a positive sign. This derivative is usually negligible for helicopters in hover (Ref. 6), consistent with its large Cramer–Rao value in the frequency domain, which indicates low sensitivity of the cost

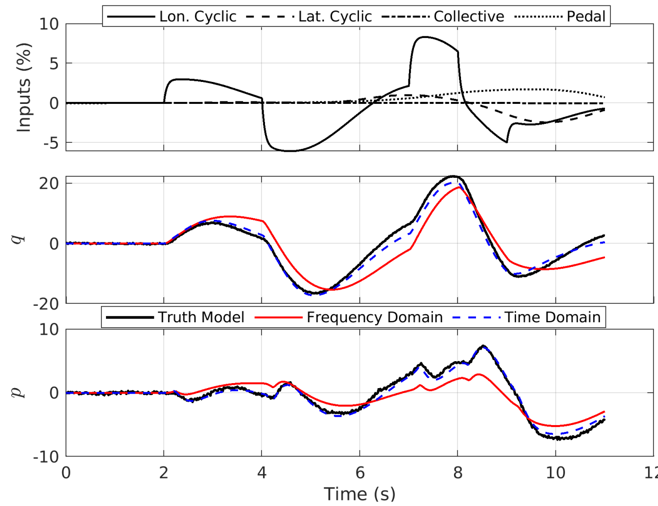

Figure 16. Comparison of the responses to longitudinal cyclic input in time domain

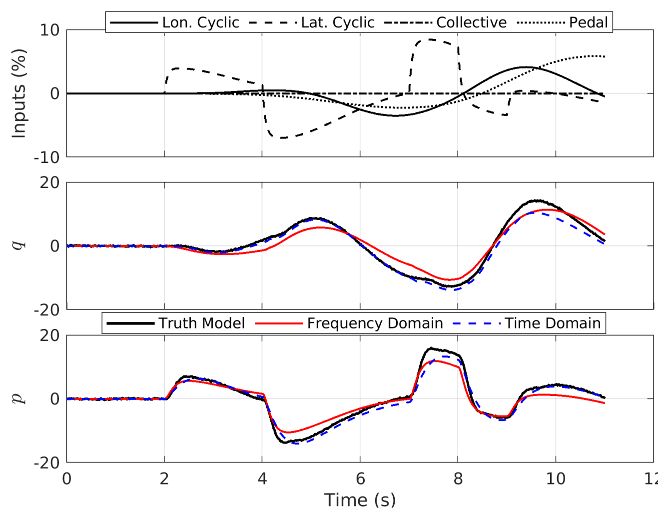

Figure 17. Comparison of the responses to lateral cyclic input in time domain

function to this parameter. Among the parameters which have small Cramer-Rao values, the identified set of parameters across the two approaches are consistent.

CONCLUSIONS

Several conclusions can be drawn from the implementation and the results obtained in this study.

1. In the transformation of flight or simulated data from time domain to frequency domain, the implementation of input conditioning is essential to obtain input-output pairs that accurately represent the interaction of each output with its corresponding input. High correlation between inputs can lead to poor conditioning, making it impossible to reliably isolate the effect of a single input on the output. This impact is evident in forward flight, where high cross-control coherence significantly

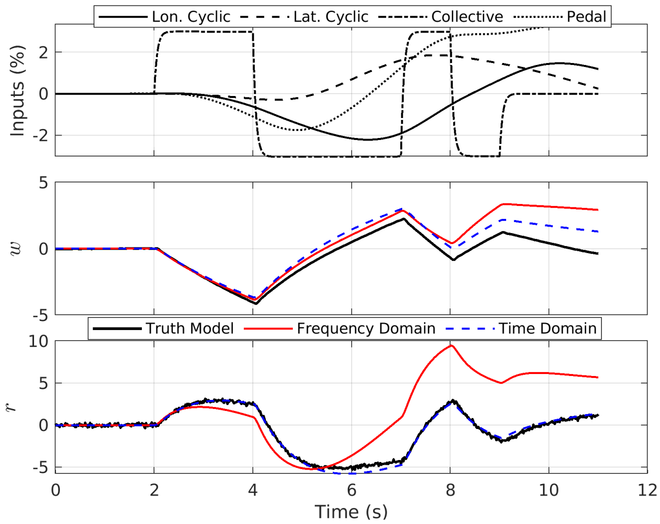

Figure 18. Comparison of the responses to collective input in time domain

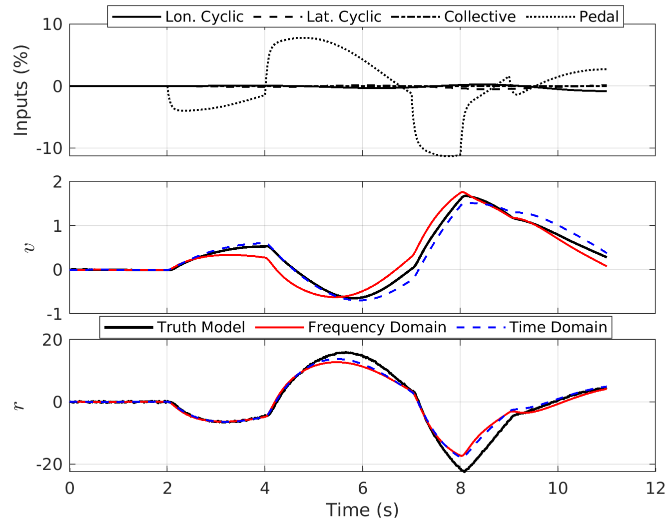

Figure 19. Comparison of the responses to pedal input in time domain

degraded estimation accuracy, resulting in generally poor outcomes and notable limitations.

2. It is crucial to evaluate not only coherence but also partial coherence to obtain a comprehensive assessment of the reliability of the results and the linear relationship between inputs and outputs.

3. Composite windowing is a key step to ensure high accuracy and resolution across the entire frequency range of interest, overcoming the inherent trade-off between window size and frequency resolution. The selection of window sizes used in composite windowing significantly influences the final frequency response signal employed for system identification.

4. Overparameterization of the transfer function may yield a good fit to the frequency response data but lack physical interpretability. Therefore, it is important to seek the minimal model order and parameter set necessary to adequately fit the signal. Furthermore, if the identification is done in frequency domain, the time domain fit must be monitored through the identification process.

5. The introduction of time delays can be particularly useful, as they capture the inherent lag between control inputs and the dynamic response of the rotorcraft without unnecessarily increasing the model complexity. However, it is important to note that improper use of time delays may lead to them compensating errors of the transfer function model, resulting in non-physical or misleading representations.

6. The definition of the unknown parameters and the choice of initial conditions have a significant impact on the accuracy of the estimation obtained, which is driven by the identification algorithm being used.

7. A systematic parameter reduction routine is required to converge on a minimal model structure. When the structure is derived through a different methodology (e.g., time domain identification), it may include parameters to which the cost function shows little sensitivity.

8. Provided that the available data are sufficient, and the model structures are comparable, time domain and frequency domain methodologies converge to similar results, yielding aerodynamic derivatives of consistent signs and comparable magnitudes.

Author contact: Natalia Cejudo Trillo natalia.cejudo@tum.de, Ongun Hazar Aslandogan ongunhazar.aslandogan@tum.de, Ilkay Yavrucuk ilkay.yavrucuk@tum.de

Table 2. Identified state derivatives in hover

Derivative	Frequency Domain	$\overline{CR}$ %	Time Domain	$\overline{CR}$ %
X_u	0.104	9.7	-0.022	3.0
X_v	0^a	-	0^a	-
X_w	0^a	-	0^a	-
X_p	0^a	-	0.042	0.8
X_q	0.205	6.4	0.049	0.9
X_r	0^a	-	0^a	-
Y_u	0^a	-	0^a	-
Y_v	-0.118	8.5	-0.149	0.6
Y_w	0^a	-	0^a	-
Y_p	0^a	-	0^a	-
Y_q	0^a	-	0^a	-
Y_r	0.132	1.6	0.075	0.7
Z_u	0^a	-	0^a	-
Z_v	0^a	-	0^a	-
Z_w	-0.354	1.1	-0.368	1.8
Z_p	0^a	-	0^a	-
Z_q	0^a	-	0^a	-
Z_r	0.117	6.1	0^a	-
L_u	0.542	5.3	0.911	2.2
L_v	-0.432	8.2	-2.446	1.3
L_w	0^a	-	0^a	-
L_p	-7.431	2.5	-3.290	1.3
L_q	2.384	2.6	2.397	1.0
L_r	0.825	3.1	0.079	5.0
M_u	-0.621	3.5	1.096	1.5
M_v	0^a	-	0^a	-
M_w	0^a	-	0^a	-
M_p	-1.987	2.7	-2.743	1.0
M_q	-0.945	3.2	-1.847	1.0
M_r	-0.461	3.2	0^a	-
N_u	0^a	-	0^a	-
N_v	-0.214	5.6	1.427	0.8
N_w	0.750	5.1	-0.083	3.8
N_p	-0.971	4.3	-0.380	3.1
N_q	-1.010	4.2	0.112	3.6
N_r	-2.540	1.1	-1.671	0.4

[a]Removed during model reduction

Table 3. Identified control derivatives in hover

Derivative	Frequency Domain	$\overline{CR}$ %	Time Domain	$\overline{CR}$ %
$X_{\delta_{lon}}$	-0.167	9.0	-0.211	0.5
$X_{\delta_{lat}}$	0^a	-	0^a	-
$X_{\delta_{col}}$	0^a	-	0^a	-
$X_{\delta_{ped}}$	0^a	-	0^a	-
$Y_{\delta_{lon}}$	0^a	-	0^a	-
$Y_{\delta_{lat}}$	0^a	-	0^a	-
$Y_{\delta_{col}}$	0^a	-	0^a	-
$Y_{\delta_{ped}}$	-0.218	1.2	-0.185	0.4
$Z_{\delta_{lon}}$	0^a	-	0^a	-
$Z_{\delta_{lat}}$	0^a	-	0^a	-
$Z_{\delta_{col}}$	-0.954	0.9	-0.861	0.5
$Z_{\delta_{ped}}$	0^a	-	0^a	-
$L_{\delta_{lon}}$	-3.954	2.4	-5.898	1.0
$L_{\delta_{lat}}$	11.466	3.7	6.696	1.1
$L_{\delta_{col}}$	0^a	-	0^a	-
$L_{\delta_{ped}}$	-2.225	1.7	-0.334	2.1
$M_{\delta_{lon}}$	4.642	1.7	5.474	0.7
$M_{\delta_{lat}}$	1.738	3.0	2.937	1.7
$M_{\delta_{col}}$	0^a	-	0^a	-
$M_{\delta_{ped}}$	0^a	-	0^a	-
$N_{\delta_{lon}}$	0^a	-	0^a	-
$N_{\delta_{lat}}$	1.887	2.4	0.869	2.5
$N_{\delta_{col}}$	2.430	1.0	1.996	0.4
$N_{\delta_{ped}}$	4.363	1.1	3.609	0.5
$\tau_{L_{\delta_{lon}}}$	0.198	3.0	0.1833	0.8
$\tau_{M_{\delta_{lat}}}$	0.101	5.6	0.117	2.8

[a]Removed during model reduction

REFERENCES

1. Tischler, M. B., "Digital control of highly augmented combat rotorcraft," Tech. rep., 1987.

2. Tischler, M. B., Fletcher, J. W., Morris, P. M., and Tucker, G. E., "Flying quality analysis and flight evaluation of a highly augmented combat rotorcraft," *Journal of Guidance, Control, and Dynamics*, Vol. 14, No. 5, 1991, pp. 954–963.

3. Aslandogan, O. H., Gursoy, G., and Yavrucuk, I., "Time Domain Identification of a Helicopter Using Minimal Representation and Time Delays," *50th European Rotorcraft Forum*, Marseille, France, 2024.

4. Tischler, M., Leung, J., and Dugan, D., "Frequency-domain identification of XV-15 tilt-rotor aircraft dynamics," *2nd Flight Testing Conference*, 1983, p. 2695.

5. Tischler, M. B., *Frequency-response identification of XV-15 tilt-rotor aircraft dynamics*, Stanford University, 1987.

6. Mark B. Tischler, R. K. R., *Aircraft and Rotorcraft System Identification*, American Institute of Aeronautics and Astronautics.

7. Greenberg, H., "A survey of methods for determining stability parameters of an airplane from dynamic flight measurements," Tech. rep., 1951.

8. Shinbrot, M., *A least squares curve fitting method with applications to the calculation of stability coefficients from transient-response data*, No. 2341, National Advisory Committee for Aeronautics, 1951.

9. He, C., Syal, M., Tischler, M. B., and Juhasz, O., "State-space inflow model identification from viscous Vortex Particle Method for advanced rotorcraft configurations," *American helicopter Society 73rd Annual Forum, Fort Worth, Texas, USA*, 2017.

10. Tischler, M. B., Fletcher, J. W., Diekmann, V. L., Williams, R. A., and Cason, R. W., "Demonstration of frequency-sweep testing technique using a Bell 214-ST helicopter," Tech. rep., 1987.

11. Tischler, M. B. and Cauffman, M. G., "Frequency-response method for rotorcraft system identification: flight applications to BO 105 coupled rotor/fuselage dynamics," *Journal of the American Helicopter Society*, Vol. 37, No. 3, 1992, pp. 3–17.

12. Lawler, M., Ivler, C., Tischler, M., and Shtessel, Y., "System identification of the longitudinal/heave dynamics for a tandem-rotor helicopter including higher-order dynamics," *AIAA Atmospheric Flight Mechanics Conference and Exhibit*, 2006, p. 6147.

13. Berger, T., Tobias, E. L., Tischler, M. B., and Juhasz, O., "Advances and Modern Applications of Frequency-Domain Aircraft and Rotorcraft System Identification," *Journal of Aircraft*, Vol. 60, No. 5, Jun 2023, pp. 1331–1353.

14. Wu, M., Lovera, M., et al., "Time-domain vs frequency-domain identification for a small-scale helicopter," *5th CEAS Specialist Conference on Guidance, Navigation and Control-EuroGNC*, 2019, pp. 1–27.

15. Tischler, M. B. and Tumashofski, C. A., "Flight Test Identification of SH-2G Flapped-Rotor Helicopter Flight Mechanics Models," *Journal of the American Helicopter Society*, Vol. 47, No. 1, 2002, pp. 18–32.

16. Seher-Weiß, S., "ACT/FHS system identification including rotor and engine dynamics," *Journal of the American Helicopter Society*, Vol. 64, No. 2, 2019, pp. 1–12.

17. Seher-Weiss, S. and von Grünhagen, W., "Comparing explicit and implicit modeling of rotor flapping dynamics for the EC 135," *CEAS Aeronautical Journal*, Vol. 5, No. 3, 2014, pp. 319–332.

18. Seher-Weiss, S., "Comparing different approaches for modeling the vertical motion of the EC 135," *CEAS Aeronautical Journal*, Vol. 6, 2015, pp. 395–406.

19. Mitchell, D., Hoh, R., He, C., and Strope, K., "Determination of maximum unnoticeable added dynamics," *AIAA Atmospheric Flight Mechanics Conference and Exhibit*, 2006, p. 6492.

20. Hoh, R. H., Mitchell, D. G., Ashkenas, I. L., Klein, R. H., and Heffley, R. K., "Proposed MIL Standard and Handbook-Flying Qualities of Air Vehicles. Volume 2. Proposed MIL Handbook," Tech. rep., 1982.

21. Engineering, A., "Aerotim Engineering Official Website," https://www.aerotim.com.tr, Accessed February 2024.

22. Bendat, J. S. and Piersol, A. G., *Random data: analysis and measurement procedures*, John Wiley & Sons, 2011.

23. Otnes, R., Enochson, L., and Maqusi, M., "Applied Time Series Analysis, Vol. 1," *IEEE Transactions on Systems, Man, and Cybernetics*, Vol. 11, No. 10, 1981, pp. 731–731.

24. Etkin, B., *Dynamics of atmospheric flight*, Courier Corporation, 2005.

25. Hess, R. A., "Aircraft and rotorcraft system identification–engineering methods with flight test examples," 2013.